Chemical Engineering Journal 154 (2009) 211–218

Contents lists available at ScienceDirect

Chemical Engineering Journal

journal homepage: www.elsevier.com/locate/cej

Modelling of diesel particulate filtration in wall-flow traps

S. Bensaid, D.L. Marchisio, D. Fino*, G. Saracco, V. Specchia

Dipartimento di Scienza dei Materiali e Ingegneria Chimica - Politecnico di Torino, Corso Duca degli Abruzzi 24, 10129 Turin, Italy

ARTICLE INFO

Article history:
Received 16 December 2008
Received in revised form 18 March 2009
Accepted 24 March 2009

Keywords:
Computational fluid dynamics
Diesel particulate filter
Soot filtration
Multiphase flow
Particle deposition
Porous media
Soot combustion

ABSTRACT

The present work addresses the modelling aspects of soot deposition inside diesel particulate filters (DPFs). These wall-flow monoliths are commonly employed in the automotive sector to reduce particulate emissions of Diesel engines. Simulations were carried out using computational fluid dynamics under different operating conditions by varying the exhaust-gas inlet velocity, the filter permeability and the soot particle size. The numerical results show that the flow field inside the filter is highly responsible for the soot distribution along the axial coordinate: the velocity of the soot laden gas through the porous wall of the bare filter is not constant along the channel, which in turn promotes an uneven deposition of particles inside the filter itself. Moreover, it has been shown that the fraction of the particles that impact the wall surface and are trapped by the porous media is sensitive to the particle size: the collection efficiency was estimated, and the most penetrating particles were found to range from 200 nm to 500 nm. The accumulation of soot particles in the porous media (depth filtration) and the subsequent formation of a soot particles layer on the top of the filter wall (cake filtration) generates an additional pressure drop. Hence, the gas through-wall velocity evolves towards an "iso-permeability" profile characterized by an almost constant soot layer thickness, since its permeability is two orders of magnitude higher than that of the bare filter. Preliminary experimental results have confirmed this behaviour. In addition, it has been shown that the velocity profile at the inlet of the filter is highly responsible for different soot loadings of the inlet filter channels.

1. Introduction

There is an established awareness of the health effects of diesel exhaust soot emissions in automotive applications [1], also considering the market expansion of diesel engines spurred by their fuel economy benefits, compared to gasoline ones. Assessments of toxicity and health effects of vehicle emissions have already shown that automotive exhausts are not only responsible for adverse effects on the respiratory and immune systems, but are also potentially carcinogenic [2]. In fact, it is almost widely accepted that soot particles emitted from diesel engines are carriers of a number of substances associated with health effects, and long-term exposure to fine particulate matter has been proven to be a risk factor for cardiovascular disease mortality, as suggested by many authors like Pope et al. [3]. Although the negative health effects are difficult to be quantified in epidemiological studies [4], several works have been carried out that focus on characterizing soot particle composition and properties, and these have been reviewed by Maricq [5] with the aim of obtaining a better understanding of the health issues and environmental footprint.

Euro V regulations fixed soot emission limits in Europe as low as 4.5 mg/km [6]. Advanced engine design is not sufficient to meet this target, therefore a tailored after-treatment device is necessary. Soot emissions can currently be reduced by physically trapping the particles with on-board diesel particulate filters (DPFs): wall-flow honeycomb monoliths have alternate plugged channels, which force the exhaust flue gases to flow through the wall. The particulate is collected on the surface of the inlet channels, thus causing an increasing pressure drop, until regeneration takes place (Fig. 1): the soot nanoparticles are first trapped in the filter porous media, resulting in a gradual modification of the filter parameters, notably porosity and permeability, as soot is collected; this phase is known as depth filtration and generally lasts a few minutes. The regions of the filter where the maximum packing density in reached then become almost "impermeable" to the particles, and a soot layer is built up on the porous filter surface. During this phase, called cake formation, the pressure drop increases linearly with time, along with the soot layer thickness. After the pressure drop has reached a maximum allowable value, entailing a too high fuel penalty, regeneration of the filter is induced by post-injecting some fuel which burns in a catalytic converter and heats the exhaust gases until the soot ignition temperature is reached. DPFs can be either catalytic or not: in the former case a catalyst is deposited onto the surface of the channel walls in order to promote soot combustion at lower tem-

* Corresponding author. Tel.: +39 011 0904654; fax: +39 011 0904699.
E-mail address: debora.fino@polito.it (D. Fino).

1385-8947/$ – see front matter © 2009 Elsevier B.V. All rights reserved.
doi:10.1016/j.cej.2009.03.043

Nomenclature

d_p particle diameter (m)

d_{pore}	filter pore diameter (m)
D_c	collector diameter (m)
E	filtration efficiency
f_D	drag coefficient
$\mathbf{g}$	gravity acceleration vector (m/s^2)
$g(\varepsilon)$	Kuwabara function
k	permeability (m^2)
N	interception coefficient
p	pressure (Pa)
ΔP	pressure drop across the filter wall (Pa)
Pe	Peclet number
s	parameter of the interception mechanism
T	temperature (K)
$\mathbf{U}$	velocity vector (m/s)
$\mathbf{U}_{c0}$	inlet velocity vector of the soot laden gas (m/s)

Greek letters

α	volume fraction
ε	porosity
η	collection efficiency
η_D	collection efficiency of the Brownian diffusion mechanism
η_R	collection efficiency of the interception mechanism
μ	viscosity (Pa s)
ρ	density (kg/m^3)

Subscripts

c	continuous phase (gas)
p	dispersed phase (particles)

peratures compared to a standard trap [7], resulting in remarkable fuel savings.

The present work addresses the modelling aspects related to soot filtration. Several approaches have been adopted in this field so far: a fundamental work has been carried out by Konstandopoulos et al. [8–10], with an approach that describes both soot filtration and filter regeneration. Soot filtration is simulated by resorting to the collection unit model, which allows to describe the loading of soot into the porous media and the consequent evolution of the filter parameters (i.e. porosity and permeability), and also simulates cake formation, whose properties (cake permeability and density) are tuned according to experimental data [8]. This model has successively been refined by investigating the micro-porous structure of the porous media by means of computer reconstruction from SEM images [9,10]. Other works have proposed 1D and 2D analytical models for the computation of the pressure drop across the filter, showing good agreement with experimental data [11,12]. Apart from the evaluation of the pressure drop, another key point is the assessment of soot collection by the filter with respect to the particle size. It is in fact foreseen that in the future Euro standards will regulate not only soot mass emissions but also the number of soot particles within a certain size range. This would entail filtration devices being tailored to this end. Experimental [13] and modelling investigations have been carried out with the specific aim of evaluating the collection efficiency of DPFs by resorting to unit cell collector models [8], analogous to a fibrous model, and their modifications taking into account the contribution due to Brownian motions, which represent the most important deposition mechanism for nano-particles [14].

An alternative approach in DPF modelling is represented by the work by Sbrizzai et al. [15], who describe soot deposition in an Eulerian–Lagrangian framework through three-dimensional computational fluid dynamics (CFD) simulations. In this work, particle tracking is directed to the evaluation of the forces acting on soot particles, which determine the particle streaklines into the clean filter channels. The soot particle streaklines and their potential impact on the deposition patterns in the DPF channels were studied, whereas filtration and collection efficiencies were not quantified. Within the more general field of particle motion in complex geometries, models of depth filtration based on a lattice-gas automata scheme have been developed, able to describe even complex phenomena like pore bridging by explicitly solving the dynamics of individual solid particles [16].

Although the "particle tracking" approach is very interesting, it is not easily applicable to the simulation of cake formation and regeneration and it is very demanding from the computational point of view. Therefore, the main aim of this work is to develop a fully predictive three-dimensional CFD model of a DPF, based on an Eulerian–Eulerian approach that overcomes most of these limitations. The proposed approach is based on three-dimensional simulations of the flow field into the filter, coupled with a sub-grid scale filtration model implemented with *User-Defined Subroutines*, in order to describe soot deposition in the filter channels and to compute the subsequent pressure drop evolution. This analysis includes the different ability of the particles to be filtered by the DPF with respect to their size. It should be pointed out that real soot particles are characterized by very large particle size distributions which range from a few nanometres to hundreds of nanometres [13]. For this reason, the simulations were carried out considering the behaviour of different populations of soot particles with characteristic sizes between 100 nm and 2 μm.

This Eulerian–Eulerian approach is particularly interesting because it could be easily coupled to a population balance equation (PBE) for the description of poly-dispersed solid–gas flows, which would result in much lower computational costs than alternative Eulerian–Lagrangian approaches. In fact, a real soot distribution could be substituted by a series of mono-dispersed particle distributions, whose size and volume fraction can be calculated by means of a very efficient algorithm [17], and/or each of these populations could be treated as an independent dispersed phase, following the so-called direct quadrature method of moments [18].

The work is outlined as follows: first, the equations governing the multiphase flow field, as well as the filtration model, are presented in Section 2. Then the system geometry, the subsequent discretization, and the different operating conditions at which the code was tested, are described in Section 3. Finally, the results of the simulations are presented and discussed in detail in Section 4.

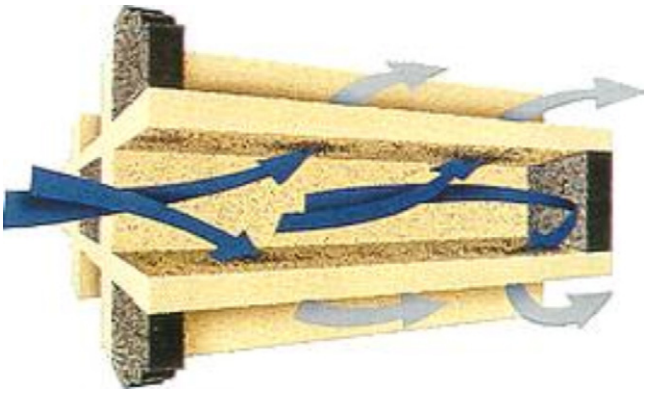

Fig. 1. Schematic of the flow inside a wall-flow monolith channel (courtesy of Dieselnet.com).

2. Governing equations

The Eulerian–Eulerian approach adopted in this work is based on the idea of describing the particulate and gaseous phases as interpenetrating media and each phase occupies a certain volume fraction α of the computational domain. The evolution of the continuous phase is governed by the continuity and the momentum balance equation, written below:

$$\frac{\partial}{\partial t}(\alpha_c \rho_c) + \nabla \cdot (\alpha_c \rho_c \mathbf{U}_c) = 0, \tag{1}$$

$$\frac{\partial}{\partial t}(\alpha_c \rho_c \mathbf{U}_c) + \nabla \cdot (\alpha_c \rho_c \mathbf{U}_c \mathbf{U}_c) = -\alpha_c \nabla p + \mu_c \nabla^2 \mathbf{U}_c + \alpha_c \rho_c \mathbf{g} + \alpha_c \frac{\alpha_p 18 \mu_c f_D}{d_p^2}(\mathbf{U}_p - \mathbf{U}_c), \tag{2}$$

where the first term on the right-hand side of Eq. (2) is the buoyancy term, the second represents the shear stresses due to the molecular viscosity of the continuous phase, the third term is the gravity acceleration, and the last term represents the interphase interaction force due to drag, expressed as a function of the slip velocity, namely the velocity difference between soot particles $\mathbf{U}_p$ and the fluid $\mathbf{U}_c$. Continuous phase equations consider the gas as incompressible, since the pressure drop under any operating condition considered in this work is too small to make this aspect relevant, unlike some different operating conditions presented in literature [9]. The quantity f_D reported in Eq. (2) represents the so-called drag coefficient and under the diluted operating conditions investigated in this work the following expression can be used, calculated according to [19]:

$$f_D = \left(1 + 0.15 Re^{0.687}\right) \tag{3}$$

Forces arising from the interaction between the particles themselves do not influence the flow field of the dispersed solid phase, since the system is very diluted. It is worth noticing that the influence of Brownian forces on the drag force via the Stokes–Cunningham coefficient, and on particle trajectories in the channels (through the addition of the Brownian diffusion coefficient in Eq. (2)) is not considered in this work, since for our particular configuration it can be neglected. In fact, the gas streamlines crossing the wall filter are responsible for the deposition location of the particles, while Brownian forces act just as a random shift, as highlighted in works with similar geometries and operating conditions [15]. However, the effect of the Brownian motions is taken into account in the calculation of the soot deposition rate onto the surface of the filtering walls through the collection efficiency η, as will become clearer below.

The deposition rate of soot into the filter walls can be calculated as a function of the local particle velocity $\mathbf{U}_p$, density ρ_p, and volume fraction α_p, as well as filter properties such as filter porosity ε, collector diameter D_c, and global collection efficiency η. The resulting transport equation for the soot volume fraction reads as follows:

$$\frac{\partial}{\partial t}\left(\alpha_p \rho_p\right) + \nabla \cdot \left(\alpha_p \rho_p \mathbf{U}_p\right) = -\alpha_p \rho_p \eta \frac{1-\varepsilon}{\varepsilon} \frac{3}{2} \frac{\left\|\mathbf{U}_p\right\|}{D_c}, \tag{4}$$

and details on the derivation of this equation can be found in [20]. If the soot particle streaklines are very close to the continuous phase ones, a faster pseudo single-phase model can be employed, in which the soot concentration is treated as a scalar quantity, and only the gas flow field is computed. In this case Eq. (4) remains unchanged, except for particle velocity $\mathbf{U}_p$, and density ρ_p, which are substituted with the corresponding ones for the gas phase, $\mathbf{U}_c$ and ρ, respectively. Details of this are discussed later in the results section. The features of the porous medium are lumped into one single parameter D_c, which represents the diameter of the fictitious spheres constituting the porous walls, which are characterized by the same particle collection efficiency of the real porous medium. The initial value of D_c is calculated as a function of the porosity and of the mean pore diameter, as described in [8].

The collection efficiency η is the probability of the successful collection of an individual soot particle on each spherical collector, and the main mechanisms contributing to soot deposition within our range of particle size are Brownian motions and interception. In the evaluation of this efficiency [8], the size of the soot particles has a considerable impact, as will be shown later. The assessment of the efficiency, and more generally of the soot deposition rate, is of great interest both in the first stages of filtration, since it is representative of the capacity of the bare filter to collect particles of various diameters, and all along the filtration process, when particle collection is enhanced by the already deposited soot cake.

The Brownian efficiency η_D (see Eq. (5)) and the interception efficiency η_R (see Eq. (6)) can be considered as independent of each other and the resulting expression of the global collection efficiency η (see Eq. (7)) can be hypothesized as follows [8]:

$$\eta_D = 3.5 g(\varepsilon) Pe^{-2/3}, \tag{5}$$

$$\eta_R = 1.5 N^2 \frac{g(\varepsilon)^3}{(1+N)^s}, \tag{6}$$

$$\eta = \eta_D + \eta_R - \eta_D \eta_R. \tag{7}$$

The Brownian motion contribution to the collection efficiency is calculated through the evaluation of the Brownian diffusivity, taking into account the deviation due to the Stokes–Cunningham coefficient C_c [14]. It is worth noticing that the Brownian efficiency η_D is a function of the Peclet number Pe and of the Kuwabara function $g(\varepsilon)$ and it depends not only on the porous media characteristics but also on the gas velocity [21]. The other contribution to the collection efficiency is given by the interception mechanism, which depends on the parameter N, namely the ratio between the particle size and the collector diameter, and on the exponent s, which is a function of the porosity [8].

As far as the pressure gradient term is concerned, the Darcy equation is adopted for the assessment of the pressure drop associated to permeation through the porous media (being modelled as isotropic):

$$\nabla P = \frac{\mu_c}{k} \mathbf{U}_c. \tag{8}$$

Since our system falls within the laminar regime, no turbulence model is needed for the solution of the governing equations and the Forchheimer term is neglected in Eq. (8), as confirmed by the literature [9,15].

The accumulation of soot particles in the filter pores modifies the characteristics of the filter as follows:

$$\varepsilon = \varepsilon_0 - \alpha_d \tag{9}$$

$$D_p = \left(\frac{1 - \varepsilon_0 + \alpha_d}{1-\varepsilon} \frac{6}{\pi}\right)^{1/3}, \tag{10}$$

$$k = k_0 \left(\frac{D_p}{D_{p0}}\right)^2 \frac{\left[2 - \frac{9}{5}(1-\varepsilon)^{1/3} - \varepsilon - \frac{1}{5}(1-\varepsilon)^2\right]}{\left[2 - \frac{9}{5}(1-\varepsilon_0)^{1/3} - \varepsilon_0 - \frac{1}{5}(1-\varepsilon_0)^2\right]} \frac{1-\varepsilon_0}{1-\varepsilon}, \tag{11}$$

where ε_0, D_{p0} and k_0 are the properties of the clean filter, while α_d is the deposited soot volume fraction [8]. During filter loading, the local porosity in the filter decreases until a minimum value is attained, corresponding to the maximum volume fraction of the soot deposited in the filter. In the regions of the filter where this limit is reached, a soot layer is built up onto the porous filter surface. This operation is modelled by setting the velocity of the dispersed phase equal to zero in the computational cells where the maximum

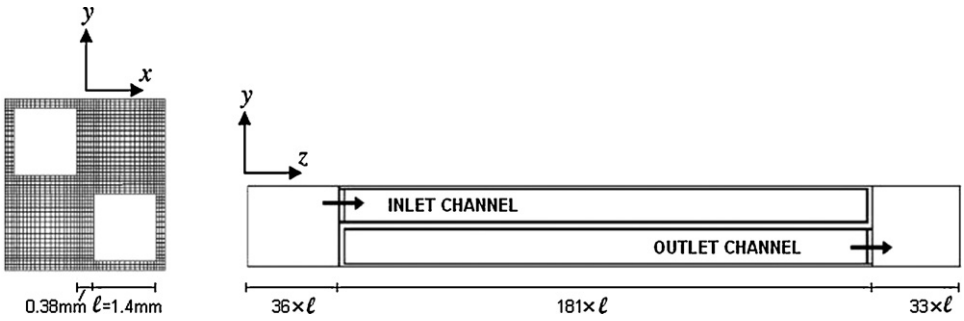

Fig. 2. Sketch of the grid used to simulate the flow field in the four channels constituting the computational domain.

soot packing limit is attained and by keeping track of the deposited soot volume fractions through *User-Defined-Memories* (UDM) [22]. Due to the uneven deposition rates inside the filter, the maximum packing limit is reached locally at different loading times. Since a pressure drop is associated to soot deposition, this modifies the through-wall velocity profile throughout the entire filtration process, as discussed in the results section.

3. Numerical details and operating conditions

The three-dimensional geometry adopted to simulate the behaviour of the system is depicted in Fig. 2. The four modelled channels are visible in the *xy* plane: two of them allow the gas to enter the filter, while the other two are plugged. At the end of the filter, the plugs are reversed, and the gas is thus forced to flow through the DPF channel walls. Before the inlet of the filter, there is an upstream region, which allows a flat velocity profile $\mathbf{U}_{c0}$ to be set. Similarly, after the filter, there is a downstream region that allows the flow to fully develop. The mesh is scaled with respect to the channel width: the lengths of the upstream region, of the filter, and of the downstream region are 36, 181 and 33 times the channel width, respectively. Each square channel is 1.4 mm in width and the filter wall is 0.38 mm in depth (see Fig. 2). The final computational domain is discretized in about 3×10^5 computational cells, thus guaranteeing a grid independent solution, which was confirmed through successive refinements of an initial grid. The lateral faces of the domain are set as periodic in order to model the behaviour of real DPFs, which are characterised by a structure of hundreds of channels (called cells) per square inch. As far as the discretization of the Navier-Stokes equations is concerned, the SIMPLE scheme was used for the pressure, while a first-order up-wind was used for the momentum.

The initial filter porosity ε_0 is set equal to 0.45, whereas its resistance coefficient $(1/k_0)$ is set equal to 2×10^{12} 1/m^2, these being typical values of Cordierite monoliths [6]. For the calculation of the collection efficiency, the mean pore diameter is supposed to be around 8.5 μm, as supported by Scanning Electron Microscopy observations, which corresponds to an initial collector diameter D_{c0} of 15.6 μm. As soot particles deposit into the porosities of the filter, the solid fraction increases until a maximum packing limit is reached: this limit was fixed at 15 kg/m^3, on the basis of experimental observations [8–10] of soot loading at similar Peclet numbers, and in particular of the values of soot particle diameter, through-wall velocity, filter porosity and pore size.

As far as the properties of soot are concerned, the cake resistance coefficient $(1/k_{cake})$ is set equal to 4×10^{13} 1/m^2 and the cake packing density is set to 100 kg/m^3, according to the experimental observations of Konstandopoulos et al. [8]. Four mono-dispersed populations of soot particles with size equal to 100 nm, 200 nm, 500 nm and 2 μm were here considered, all having a typical solid volume fraction of 5×10^{-8} (which represents almost 50 mg$_{soot}$/kg$_{gas}$ when the soot density ρ_p is assumed to be nearly 1000 kg/m^3). The gaseous flow has a density equal to 1.225 kg/m^3 and a viscosity of 1.7894×10^{-5} Pa s, since the simulations are then compared to experimental results obtained by loading a filter with a soot laden flow of air, at ambient temperature (see next section). Simulations are carried out under laminar flow conditions, as the gas is fed at $\mathbf{U}_{c0}$ = 3 m/s in the reference case, even though the effect of the inlet velocity $\mathbf{U}_{c0}$ on the pressure drop and on the soot par-

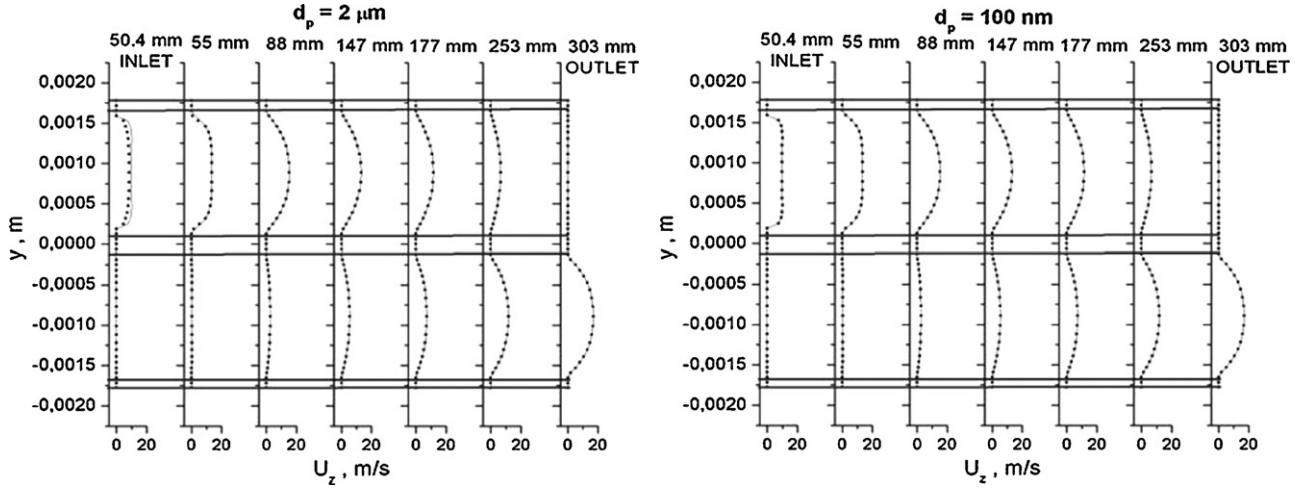

Fig. 3. Axial velocity profiles at different axial coordinates of the channel for gas (solid line) and soot particles (dots) for d_p = 2 μm (top) and 100 nm (bottom), $\mathbf{U}_{c0}$ = 3 m/s and for $1/k = 2 \times 10^{12}$ 1/m^2.

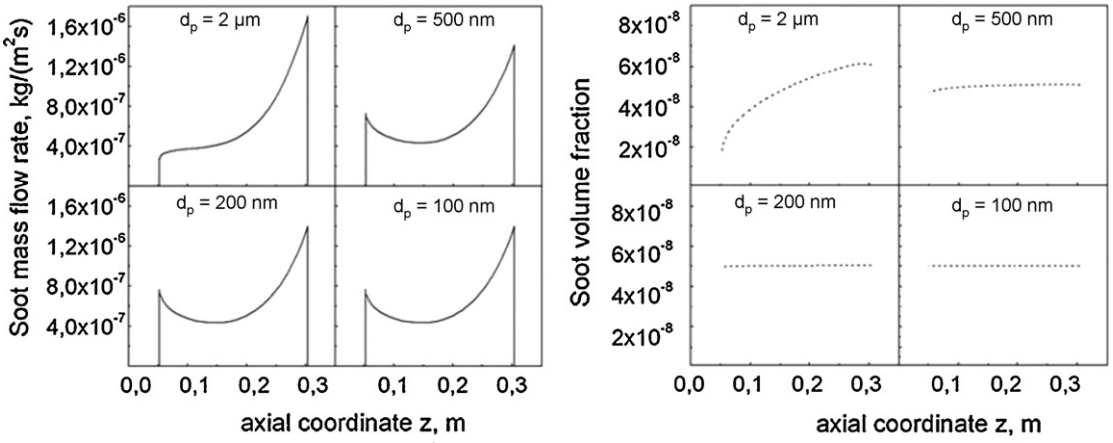

Fig. 4. Soot mass flow rate and soot volume fraction at the wall surface along the axial coordinate for $\mathbf{U}_{c0} = 3$ m/s, $1/k = 2 \times 10^{12}$ 1/m^2 and for different soot particle sizes ($d_p = 2$ μm, 500 nm, 200 nm, and 100 nm).

ticles flow field is enlightened by simulating the behaviour of the multi-phase flow also at 5.85 m/s.

4. Results and discussion

Fig. 3 shows the profiles of the axial velocity for air and soot particles at different axial positions in the channel, at the beginning of the soot filtration process (bare filter). The cases with a particle size equal to 100 nm and 2 μm are here depicted, with $\mathbf{U}_{c0}$ equal to 3 m/s and a filter resistance of 2×10^{12} 1/m^2. Since the computational domain includes an upstream region, the channel length runs from an axial coordinate equal to 50.5 mm up to 303.8 mm, which represents the filter outlet. As expected, the soot particles follow the gas streaklines in any region of the channel, except for the one close to inlet, where appreciable inertial effects occur, especially for large particles. These results are in good agreement with previous works carried out on the same geometry [15] by using an Eulerian–Lagrangian approach. It is interesting to point out that the Eulerian–Eulerian approach proposed in this work is characterized by much lower computational costs and can be easily extended to the subsequent filtration steps (namely soot deposition in the porous media of the filter, soot cake formation and regeneration) as well as to the treatment of poly-dispersed particulate systems.

If one computes the static pressure drop calculated on the wall surface at the inlet and outlet channel sides, with respect to the axial coordinate, it appears that the velocity of both phases through the filter wall is not constant along the axial direction. In fact, the through-wall velocity on the wall surface presents a minimum at about 40% of the channel length, which is in excellent agreement with the results presented in [15].

Fig. 4 reports the soot mass flow rate (left) as well as the soot volume fraction (right) on the wall surface along the axial coordinate. Inertial effects may occur for large particles, resulting in a velocity difference between the two phases and an uneven soot volume fraction distribution along the channel, even when a constant solid volume fraction of 5×10^{-8} enters the filter. These inertial effects, as expected, disappear almost completely for particles smaller than 500 nm and the soot volume fraction becomes constant along the axial coordinate and equal to the inlet value. Therefore, for very small particles, the soot mass flow rate (see left side of Fig. 4) has the same profile as the gas through-wall velocity and it is just scaled by the soot mass concentration. It is worth noticing that the effect of soot entrainment at the inlet of the channel is more and more evident as the inlet velocity increases and although several values were Investigated. For the sake of brevity only the results for $\mathbf{U}_{c0} = 5.85$ m/s are presented in Fig. 5. As seen, a higher inlet velocity results in a more uneven soot distribution along the channel length, although it does not prevent soot from crossing the filter wall at any part of the inflow region involved in the *vena contracta*.

The calculated inertial effects suggest that simulations of real diesel soot populations (diluted system of particles with almost all diameters below 500 nm) can be carried out within a pseudo-single phase framework, for these particular operating conditions. Particle concentration can be treated as a scalar quantity, using a balance

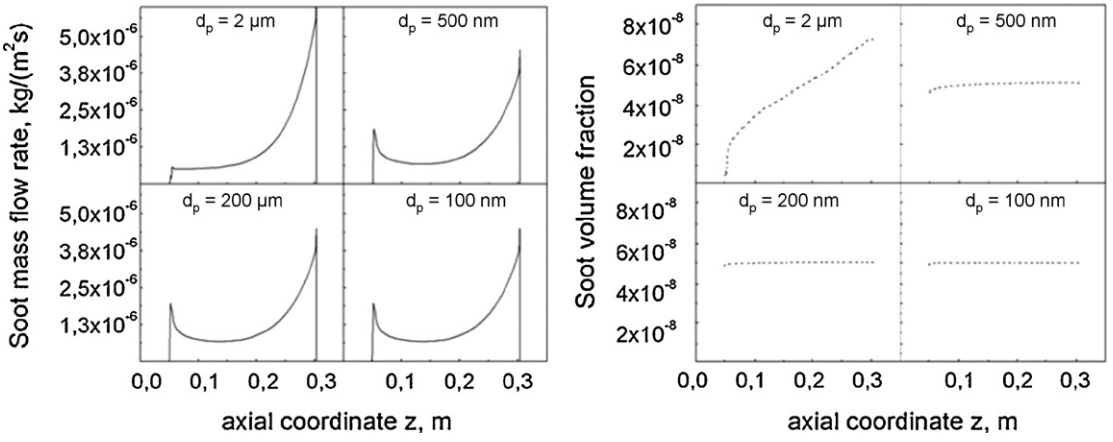

Fig. 5. Soot mass flow rate and soot volume fraction at the wall surface along the axial coordinate for $\mathbf{U}_{c0} = 5.85$ m/s, $1/k = 2 \times 10^{12}$ 1/m^2 and for different soot particle sizes ($d_p = 2$ μm, 500 nm, 200 nm, and 100 nm).

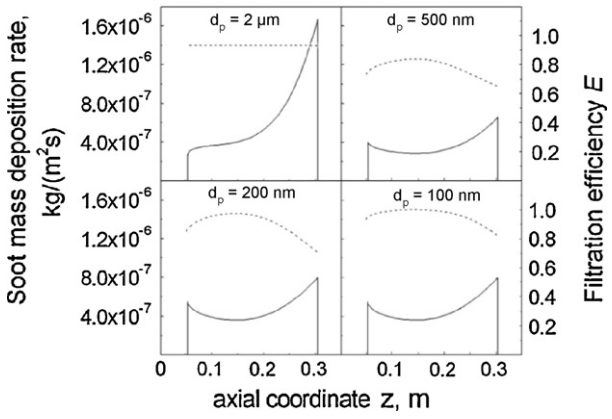

Fig. 6. Soot mass deposition rate at the wall surface (left axis/solid line) and soot filtration efficiency E (right axis/dotted line) along the axial coordinate for $\mathbf{U}_{c0} = 3$ m/s, $1/k = 2 \times 10^{12}$ 1/m^2 and for different soot particle sizes ($d_p = 2$ μm, 500 nm, 200 nm, and 100 nm).

equation with a generation term similar to the one in Eq. (4), but with the soot particle velocity $\mathbf{U}_p$ equal to the one of the gas phase's one $\mathbf{U}_c$, and a convective term which becomes zero in the computational cells where soot volume fraction (the scalar) has reached the maximum packing limit. This leads to a faster computation of time-dependent soot loading and cake formation. It should be pointed out that different engine operating conditions could lead to lower limits of the particle size at which inertia become negligible, for instance when high inlet velocities $\mathbf{U}_{c0}$ occur, and the two-phase model can be conveniently used in these cases.

The results reported so far refer to soot particle distributions and deposition rates along the channel length but not on the real amounts of soot filtered. In order to estimate these quantities it is crucial to properly calculate the global collection efficiency η, which is a function of the gas and soot properties, notably gas temperature and soot particle size and velocity. A closer observation of Eq. (7) highlights that the global collection efficiency results from the contributions due to Brownian motions and interception (i.e., η_D and η_R, respectively) and presents a minimum between 200 and 500 nm, under the operating conditions investigated in this work. This minimum arises since very small particles are efficiently collected by deposition due to Brownian forces, whereas larger particles are collected in the filter pores due to the interception mechanism. The collection efficiency is also influenced by the value of the through-wall velocity via the Peclet number (see Eq. (5)), therefore its value changes with respect to the axial coordinate. In order to quantify the ability of a generic filter of depth L to collect soot particles, it is very convenient to calculate an "integral" filtration efficiency E, defined as the integral along the filter depth on the right hand side of Eq. (4) at a steady state, which results in:

$$E = 1 - \exp\left(-\eta \frac{1-\varepsilon}{\varepsilon} \frac{3}{2} \frac{L}{D_c}\right). \quad (12)$$

This filtration efficiency represents the volume (or mass) fraction of the incoming soot particles that are collected by the clean filter. The expression in Eq. (12) is no longer valid when the filter is laden with particles, since the properties of the filter have changed according to the soot volume fraction calculated in each computational cell of the filter domain (along the axial coordinate, and especially along the thickness of the wall itself). The integral filtration efficiency E (for a filter depth L of about 0.38 mm) and the actual "soot mass deposition rate" (namely the rate of soot filtered by the filter walls per unit of filtration area) are reported along the axial coordinate in Fig. 6. By comparing these axial profiles with the soot mass flow rates reported in Fig. 4, it is clear that larger particles ($d_p = 2$ μm) are completely filtered by the filter walls, while the filtration efficiency E is lower than unity for smaller particles, in particular in the regions where the through wall velocity is high (see Fig. 6). Higher efficiencies are only obtained when a soot layer is formed on the filter walls in the successive filtration steps [8,13].

However, the situation presented in Fig. 6 is valid for the clean filter. As soot particles are trapped into the filter walls the filter characteristics change to a great extent. In particular, the porosity of the filter decreases, whereas the collector diameter increases, resulting in different flow fields for the soot particles and the gas phase and in

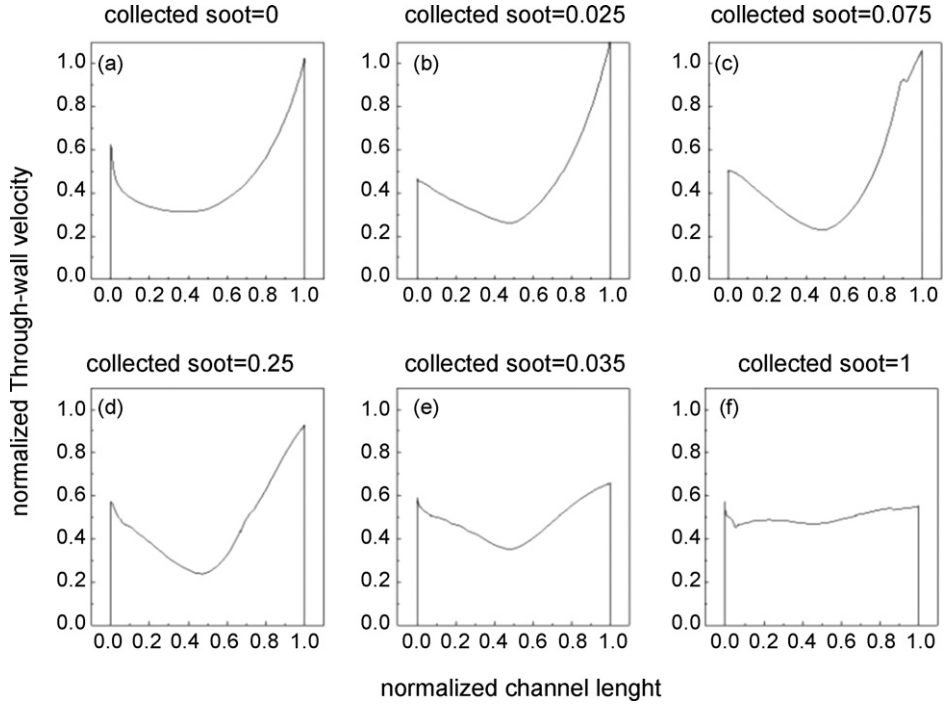

Fig. 7. Normalized through-wall gas velocity at different instants corresponding to different amounts of normalized soot collected volume fractions for $d_p = 100$ nm.

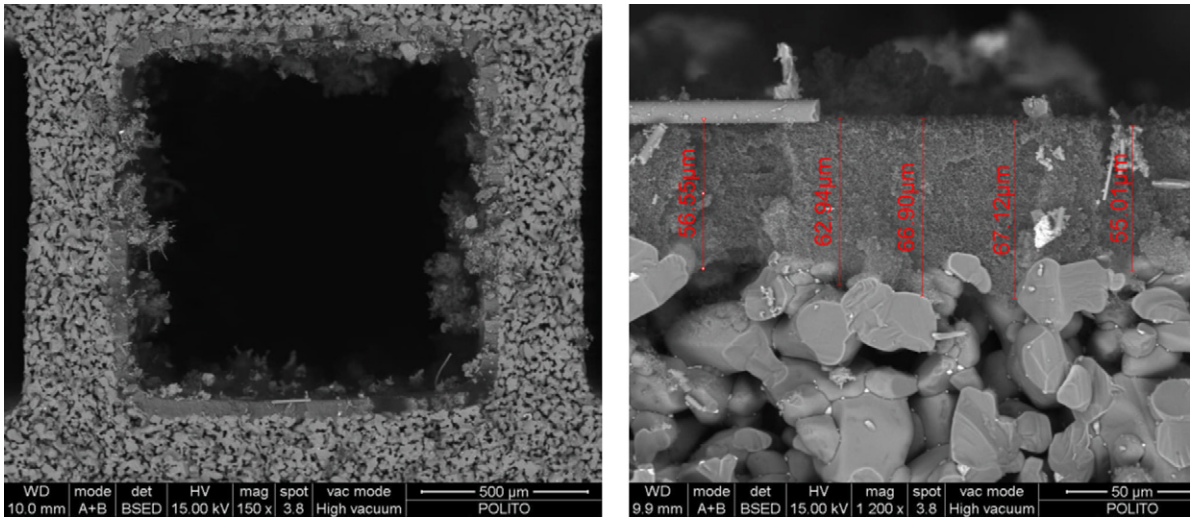

Fig. 8. Thickness of the soot layer along the filter, measured (SEM figure) at the mid point of inlet channel 7 (face at $z = 2$ cm): 150× and 1200×.

higher global filtration efficiencies. Moreover, after the soot volume fraction deposited in the pores of the filter has reached the maximum packing limit, the cake starts to build up, and an additional contribution to the total pressure drop is generated, which again affects the flow field of both the continuous and dispersed phases. For the sake of brevity, only the case of a characteristic particle size of 100 nm is here presented and discussed, as this size is much more representative of the particle size of modern common-rail diesel engines. At the beginning of the filtration operation (Fig. 7a), the through-wall velocity of the gas corresponds to the profile in Fig. 4 for 100 nm. It then changes as a consequence of soot loading: the most involved regions are at the ends of the channel, close to the inlet and close to the plug (Fig. 7b), where the highest deposition rates occur. As filtration proceeds, soot reaches the maximum packing limit inside the porosities of the filter and the cake starts building (Fig. 7c), creating a pressure drop which is highlighted by the decrease in the through-wall velocity. As the cake grows with time, the through-wall velocity profile becomes flatter and flatter (Fig. 7d–f), corresponding to a more or less constant cake thickness along the axial coordinate.

In conclusion, some preliminary experimental results are presented in order to compare the behaviour of simulated axial profiles of the normalized cake thickness with real ones. The tested filter has 300 cpsi, is 17.7 cm long and 2.54 cm in diameter. The filter was canistered with vermiculite in a 4 cm diameter pipe, and was loaded through a synthetic soot generator (Aerosol Generator GFG-1000-PALAS) at a flow rate of 46 l/min. A conic surface joined the gaseous inlet pipe (6 mm in diameter, connected to the soot generator) to the 4 cm pipe. The soot concentration was 5 mg/h, and loading lasted 24 h. The inlet velocity was not constant at the front cross sectional area, since there is a strong maldistribution at the inlet of the filter and each channel experienced a different velocity. The flow into the central channels was higher due to the persistence of a gas jet, generated in correspondence to the 6 mm pipe outflow, and not dissipated in the cone. These phenomena also occur in real full scale DPFs, since the adduction pipe is far smaller than the diameter of the monolith and an uneven distribution of the gas in the channels occurs.

In order to verify such behaviour, the cake thickness inside the channels has been evaluated from SEM images, thus obtaining a mean value from local measurements (Fig. 8). The measurements include channels from the centre to the periphery of the filter, each one evaluated at different axial positions: this was done by cutting the filter into segments, while still preserving the structure of the layer as can be seen in Fig. 8. When comparing channels at the same axial position (the channels are named 1 to 4 from the centre to the periphery in Fig. 9-right) it appears that the lateral channels are poorly loaded, while the central one

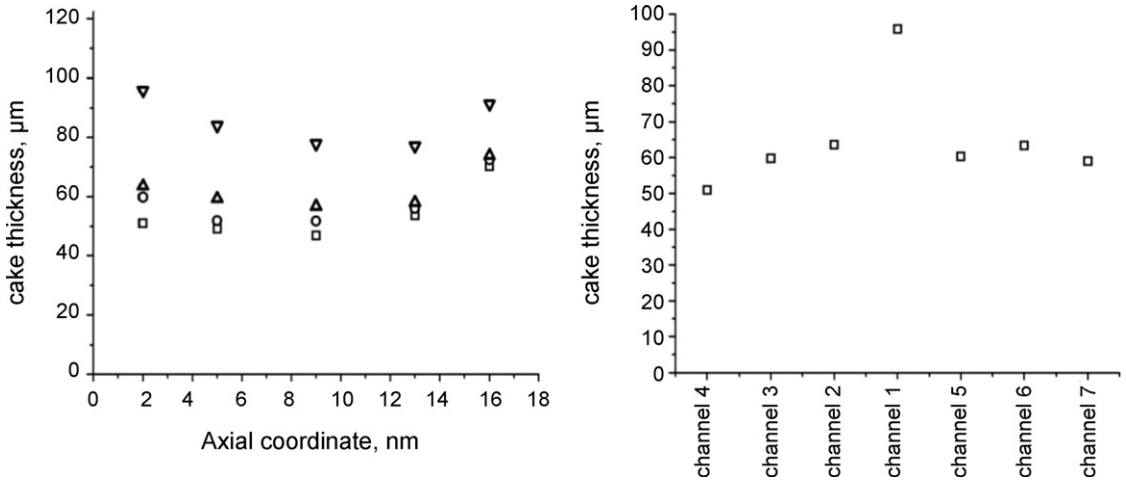

Fig. 9. Experimental thickness of the soot layer along the filter. Left: different axial positions (reverse triangles, channel 1; triangles, channel 2; circles, channel 3; squares, channel 4); right: channel locations (face at $z = 2$ cm).

is considerably involved in soot filtration, the cake being almost twice as thick. Instead, if one focuses on the thickness in a single channel, at different axial positions (Fig. 9-left), the behaviour predicted by the simulations is confirmed by the experimental results. Hence, in channel 1 (central one) the cake has a minimum thickness at around half of the total filter length, while the edges are more heavily loaded since there the velocity is higher. In the other channels (2-3-4), whose profiles are similar, the soot cake is thinner and there is less variation along the axial coordinate, indicating a lower through-wall velocity, due to a poor inlet flow. These considerations suggest the importance of coupling the single channel model described so far with a higher scale model (namely a full scale DPF model) which is able to correctly describe the flow field in front of the filter inlet, and therefore to predict the amount of deposited soot inside the channels at a certain location. This information is particularly important during soot combustion if filter regeneration is tackled [7], since excessive concentrations of soot must be predicted and avoided in order not to generate high heat release and so cracks or melting of the porous support.

5. Conclusions

A model for the description of soot filtration through DPFs has been presented and discussed. Particle deposition was found to be influenced mainly by the gas through-wall velocity, the soot volume fraction and the filtration efficiency.

The through-wall velocity values are maximum at the inlet and at the outlet of the channel, while they are at a minimum for approximately 40% of the total channel length. The computation of the through-wall velocity along the axial coordinate for decreasing permeabilities results in a flatter and flatter profile, while the opposite behavior occurs if the inlet velocity in the DPF is increased.

The second factor is represented by the soot volume fraction, which enters the filter at a constant value and, due to the inertial effects of soot particles, assumes an uneven profile at different axial positions. The inertial contribution to the flow of the dispersed phase can be detected above 500 nm, whereas it is negligible for smaller particles.

The last factor is the filtration efficiency, which depends on both the above mentioned through-wall velocity and particle size. Velocity has a negative effect on soot collection, since it decreases the capacity of the filter to trap soot particles due to the Brownian diffusion. Particle size is also very important in the evaluation of particle filtration, and the most penetrating particle sizes were found to be between 200 and 500 nm.

The progressive deposition of particles into the porous filter walls (depth filtration) and the formation of a superficial soot layer (cake formation) modified both the filtration efficiency and the spatial distribution of soot inside the filter. The cake layer assumed an almost constant thickness for high soot loadings, since the high viscous resistance of such a layer flattered the through-wall velocity profiles.

An exhaustive experimental campaign over a wide range of operating conditions is currently ongoing for validation purposes, which in particular is related to the physical properties of the deposited soot. At present, preliminary experimental results showed the peculiar shape of the deposited soot, which is at a minimum at around half of the filter length. However, the measurements have highlighted the importance of coupling the single channel model to a full scale DPF model, which is able to compute the real inlet velocity in the channels, since they are exposed to an uneven inlet flow.

References

[1] H.G. Neumann, Health risk of combustion products: toxicological considerations, Chemosphere 42 (2002) 473–479.
[2] S.H. Ye, W. Zhou, J. Song, B.C. Peng, D. Yuan, Y.M. Lu, P.P. Qi, Toxicity and health effects of vehicle emissions in Shanghai, Atmospheric Environment 34 (1999) 419–429.
[3] C.A. Pope III, R.T. Burnett, G.D. Thurston, M.J. Thun, E.E. Calle, D. Krewski, J.J. Godleski, Cardiovascular mortality and long-term exposure to particulate air pollution, Circulation 109 (2004) 71–77.
[4] N. Englert, Fine particles and human health–a review of epidemiological studies, Toxicology Letters 149 (2004) 235–242.
[5] M.M. Maricq, Chemical characterization of particle emissions from diesel engines, A Review Journal of Aerosol Science 38 (2007) 1079–1118.
[6] www.dieselnet.com.
[7] N.K. Labhsetwar, A. Watanabe, T. Mitsuhashi, New improved syntheses of $LaRuO_3$ perovskites and their applications in environmental catalysis, Applied Catalysis B: Environmental 40 (1) (2003) 21–30.
[8] A.G. Konstandopoulos, E. Skaperdas, E. Papaioannou, D. Zarvalis, E. Kladopoulou, Fundamental studies of diesel particulate filters: transient loading, regeneration and aging, SAE 2000-01-1016, 2000.
[9] A.G. Konstandopoulos, Flow resistance descriptors for diesel particulate filters: definitions, measurements and testings, SAE 2003-01-0846, 2003.
[10] A.G. Konstandopoulos, M. Kostoglou, N. Vlachos, E. Kladopoulou, Progress in diesel particulate filter simulation, SAE 2005-01-0946, 2005.
[11] A. Suresh, A. Khan, J.H. Johnson, An experimental and modelling study of cordierite traps—pressure drop and permeability of clean and particulate loaded traps, SAE 2000-01-0476, 2000.
[12] Z. Zang, S.L. Yang, J.H. Johnson, Modeling and numerical simulation of diesel particulate trap performance during loading and regeneration, SAE 2002-01-1019, 2002.
[13] E. Wirojsakunchai, E. Schroeder, C. Kolodziej, D.E. Foster, N. Schmidt, T. Root, T. Kawai, T. Suga, T. Nevius, T. Kusaka, Detailed diesel exhaust particulate characterization and real-time DPF filtration efficiency measurements during PM filling process, SAE 2007-01-0320, 2007.
[14] E. Ohara, Y. Mizuno, Y. Miyairi, T. Mizutani, K. Yuuki, Y. Naguchi, T. Hiramatsu, M. Makino, A. Takahashi, H. Sakai, M. Tanaka, A. Martin, S. Fujii, P. Busch, T. Toyoshima, T. Ito, I. Lappas, C.D. Vogt, Filtration behaviour of diesel particulate filters (1), SAE 2007-01-0921, 2007.
[15] F. Sbrizzai, P. Faraldi, A. Soldati, Appraisal of three dimensional numerical simulation for sub-micron particle deposition in a micro-porous ceramic filter, Chemical Engineering Science 60 (2005) 6551–6563.
[16] M.J. Biggs, S.J. Humby, A. Buts, U. Tuzun, Explicit numerical simulation of suspension flow with deposition in porous media: influence of local flow field variation on deposition processes predicted by trajectory methods, Chemical Engineering Science 58 (2003) 1271–1288.
[17] D.L. Marchisio, R.O. Fox, Multiphase Reacting Flows: Modelling and Simulation, 492, Springer Verlag, 2007.
[18] D.L. Marchisio, R.O. Fox, Solution of population balance equations using the direct quadrature method of moments, Journal of Aerosol Science 36 (2005) 43–73.
[19] L. Schiller, Z.Z. Naumann, Ver. Deutsch. Ing. 77 (1935) 318.
[20] L.S. Fan, C. Zhu, Principles of Gas-solid Flows, Cambridge Univ. Press, Cambridge, 1998.
[21] K.W. Lee, J.A. Gieseke, Collection of aerosol particles by packed beds, Environmental Science & Technology 13 (4) (1978) 1761.
[22] S. Bensaid, D.L. Marchisio, D. Fino, G. Saracco, V. Specchia, Proc. of the 10th World Filtration Congress, Leipzig, 2008, pp. 328–332.